

# Exploring the effects of diffuse ionised gas in two local analogues of high-redshift star-forming galaxies

P. Lagos<sup>1,2</sup>, A. Nigoche-Netro<sup>3</sup>, T. C. Scott<sup>2</sup>, C. Sengupta<sup>4,5</sup>, and R. Demarco<sup>1</sup>

<sup>1</sup> Institute of Astrophysics, Facultad de Ciencias Exactas, Universidad Andrés Bello, Sede Concepción, Talcahuano, Chile

<sup>2</sup> Instituto de Astrofísica e Ciências do Espaço, Universidade do Porto, CAUP, Rua das Estrelas, 4150-762 Porto, Portugal  
e-mail: Patrício.Lagos@astro.up.pt

<sup>3</sup> Instituto de Astronomía y Meteorología, Universidad de Guadalajara, Guadalajara, Jal. 44130, México

<sup>4</sup> Centre for Space Research, North-West University, Potchefstroom 2520, South Africa

<sup>5</sup> National Institute for Theoretical and Computational Sciences (NITheCS), Potchefstroom 2520, South Africa

Received September 15, 1996; accepted March 16, 1997

## ABSTRACT

**Aims.** We investigate the impact of diffuse ionised gas (DIG) on the determination of emission line ratios and gas-phase metallicities in two local analogues of high-redshift star-forming galaxies: UM 462 and IIZw 40. Understanding how DIG affects these quantities is essential for interpreting unresolved observations of distant galaxies, where integrated spectra are often used to trace their chemical evolution.

**Methods.** Using archival Very Large Telescope, Multi-Unit Spectroscopic Explorer (MUSE) data, we spatially resolved the warm ionised medium of both galaxies. We derived oxygen abundances through the direct method and several HII-based strong-line calibrators, and we used the H $\alpha$  surface brightness ( $\Sigma(H\alpha)$ ) to distinguish regions dominated by HII or DIG emission.

**Results.** Oxygen abundances derived from the N2 and O3N2 indices show an inverse correlation with  $\Sigma(H\alpha)$ , ionisation parameters, and H $\alpha$  equivalent width (EW(H $\alpha$ )), with DIG-dominated regions exhibiting  $12 + \log(O/H)$  values higher than the mean for their galaxy by  $\sim 0.2$  dex in UM 462 and  $\sim 0.1$  dex in IIZw40. The metallicity differences derived from these strong-line calibrators reach about 0.4 dex and 0.3 dex between the highest (HII-dominated) and lowest (DIG-dominated)  $\Sigma(H\alpha)$  bins in UM 462 and IIZw40, respectively. We found a linear correlation between  $\Delta(O/H)$  (O/H deviation from the mean interstellar medium value) and EW(H $\alpha$ ). Trends with  $\Sigma(H\alpha)$ , metallicity, EW(H $\alpha$ ), and ionisation parameter suggest smoothly evolving ionisation conditions in the interstellar medium in our galaxies. Such trends and metallicity variations derived from HII-based calibrators reflect different ionisation sources and levels rather than true abundance changes. In particular, the use of these calibrators can lead to spurious metallicity gradients in galaxies with extended DIG tails, such as tadpole or cometary-like galaxies, which can be misinterpreted as evidence of the infall of metal-poor gas. The most likely mechanism for ionising the DIG in our sample of HII or BCD galaxies is the leakage of photons from HII regions, with shocks induced by stellar feedback processes also contributing significantly. Consequently, such contamination may affect the reliability of the derived oxygen abundances. Our results highlight the importance of accounting for DIG in galaxy metallicity estimates since it potentially biases metallicity gradient measurements. This is particularly relevant for large surveys at high redshift that rely on integrated galaxy spectra.

**Key words.** Galaxies: dwarf – Galaxies: individual: UM 462 – Galaxies: individual: IIZw40 – Galaxies: abundances – Galaxies: ISM

## 1. Introduction

Local star-forming galaxies, such as dwarf HII galaxies and/or blue compact dwarfs (BCDs), are critical for understanding the processes that shaped galaxies in the early Universe. These nearby systems, with their intense star formation, low mass, and low metallicities, closely resemble galaxies that existed in the early Universe. By studying these local systems, we can better interpret the physical conditions and evolutionary processes of their high-redshift counterparts. Notably, such investigations create a vital connection between the detailed phenomena observable in the local Universe and the broader picture over cosmic time of galaxy formation revealed by large ground- and space-based telescopes, such as the *Hubble* Space Telescope (HST; e.g. Beckwith et al. 2006) and more recently the *James Webb* Space Telescope (JWST; e.g. Sanders et al. 2023).

The warm ionised component of the interstellar medium (ISM) in star-forming galaxies can be divided into two main

components: HII regions, where hydrogen is fully ionised by young and massive stars, and the diffuse ionised gas (DIG), a more extended, lower-density component outside of HII regions characterised by lower H $\alpha$  surface brightness ( $\Sigma(H\alpha)$ ). There are several likely mechanisms responsible for ionising the DIG, including (i) Lyman escape photons from the HII regions (e.g. Giammanco et al. 2004), (ii) shock ionisation driven by stellar winds and/or outflows (e.g. Dopita & Sutherland 1995; Tüllmann & Dettmar 2000; Allen et al. 2008; López-Cobá et al. 2020) in star-forming galaxies, (iii) photoionisation from hot low-mass evolved stars (HOLMES) or post-asymptotic giant branch (post-AGB) stars in retired galaxies and regions within them (e.g. Stasińska et al. 2008; Singh et al. 2013; Lacerda et al. 2018; Lagos et al. 2022), (iv) turbulent mixing layers (Rand 1998; Binette et al. 2009), and (v) cosmic rays (Wiener et al. 2013), among others. Several methods have been developed and used to segregate HII- and DIG-dominated regions or to account

for DIG contamination (e.g. Kaplan et al. 2016; Lacerda et al. 2018; Sánchez 2020; Sánchez et al. 2021; Metha et al. 2022; Lugo-Aranda et al. 2024). However, the broader impact of these two regimes on galaxy properties at different redshifts remains unclear (e.g. Zhang et al. 2017; Tomičić et al. 2021).

The DIG affects the emission line ratios such as [NII]/H $\alpha$ , [SII]/H $\alpha$ , and [OIII]/H $\beta$ , which tend to increase with distance from the galaxy centre, thereby influencing the inferred gas-phase metallicity and the corresponding gradients obtained from strong-line methods (e.g. Vale Asari et al. 2019). Strong-line methods (e.g. Pettini & Pagel 2004; Marino et al. 2013), which are used to derive metallicity, are calibrated using the direct method (measurement of the electron temperature  $T_e$ ), photoionisation models (e.g. Kewley & Dopita 2002), or a combination of both (e.g. Denicoló et al. 2002). Moreover, the stellar mass-star formation rate relation (e.g. Mannucci et al. 2010) should be interpreted with care, as the star-formation rate derived from L(H $\alpha$ ) may be biased due to DIG contamination. These emission line ratios are also affected by the relative strength of the DIG and HII emission (Poetrodjojo et al. 2019), but observations usually lack sufficient resolution to clearly distinguish DIG- from HII-dominated regions.

The ionised gas in HII galaxies and BCDs show complex and, in some cases, turbulent kinematic features (e.g. Bordalo et al. 2009; Moiseev & Lozinskaya 2012) as well as filamentary structures, shells, and cavities resulting from the kinetic energy of stellar winds and supernova explosions and features arising from flyby interactions (e.g. Scott et al. 2024), which makes distinguishing and separating the HII- and DIG-dominated regions very challenging. In fact, most of the stellar tails in our sample of cometary and/or extremely metal-poor (XMP;  $12 + \log(O/H) \lesssim 7.6$ ) BCDs (Papaderos et al. 2008) are co-spatial with an extended DIG component (Lagos et al. 2016; Papaderos & Östlin 2012; Lagos et al. 2014, 2018). The presence of DIG may significantly influence the physical and chemical properties of these galaxies.

In this paper we use archival Very Large Telescope (VLT), Multi-Unit Spectroscopic Explorer (MUSE) data from two local HII and/or BCD galaxies (UM 462 and IIZw40) to investigate these issues and gain insights into the processes ionising the DIG and their impact on integrated galaxy properties. The MUSE spatial sampling is  $\sim 12$  pc and  $\sim 10$  pc per pixel or spaxel for UM 462 and IIZw40, respectively, which is sufficient to distinguish between DIG- and HII-dominated regions. The structure of this article is as follows: Section 2 presents the observations, data reduction, and spectral fitting used in this study. In Sect. 3 we describe our results as well as the DIG definition, the determination of emission line ratios, ionisation parameters, and oxygen abundances. Finally, in Sect. 4 we present a discussion and summarise our conclusions.

## 2. Observations, data reduction, and spectral fitting

Our two BCD galaxies are from Lagos et al. (2007), and they were selected for their extended ionised gas regions and differences in the strength of the current starburst. IIZw40 is undergoing a strong starburst arising from an ongoing merger, while UM 462 is relatively unperturbed (van Zee et al. 1998). Both galaxies have archival ESO VLT, MUSE (Bacon et al. 2010) data. UM 462 was comprehensively analysed by Monreal-Ibero et al. (2023), while Marasco et al. (2023) analysed only the kinematics of UM 462 and IIZw40. The corresponding ID programs are 0101.A-0282(A) for UM 462 and 094.B-0745(A) for IIZw40. The MUSE observations were made in wide-field mode,

with a  $1' \times 1'$  field of view. This setup covers a spectral range of  $\sim 4800$ – $9300$  Å, with spatial and spectral sampling of  $0.2''$  per spaxel and  $1.25$  Å, respectively. Offset sky observations enabled us to perform effective sky subtraction. Table 1 summarises the galaxy parameters and observing log. Data were processed using the MUSE pipeline (v2.6.2; Weilbacher et al. 2020), which included bias correction, wavelength calibration, cube assembly, heliocentric correction, sky subtraction, and exposure merging. The resulting data cubes were further corrected for redshift and Galactic extinction using the reddening law from Cardelli et al. (1989). See Lagos et al. (2022) for further details.

**Table 1.** General parameters of our sample galaxies and observing log.

	UM 462	IIZw40
RA(J2000)	11h52m37.1926s	05h55m42.6147s
Dec(J2000)	-02d28m09.907s	+03d23m31.657s
Av <sup>a</sup> (mag)	0.127	2.260
D (Mpc)	12.55	10.33
Scale (kpc/arcsec)	0.061	0.050
z	0.003469	0.002682
12+log(O/H)	8.02 <sup>b</sup>	8.07 <sup>c</sup>
Date of observation	2018-04-17	2014-12-29
Exp. time	4x500 s	3x960 s
Mean airmass	1.08	1.22

**Notes.** The top rows show the general parameters of our sample from NED. The lower rows contain observing log information.

<sup>(a)</sup> Galactic extinction from Schlafly & Finkbeiner (2011). <sup>(b)</sup> (Monreal-Ibero et al. 2023). <sup>(c)</sup> (Bordalo & Telles 2011).

The stellar continuum was removed based on the spectral synthesis code FADO (Gomes & Papaderos 2017) version V1.B, with SSP templates from Bruzual & Charlot (2003), metallicities  $Z = 0.004$ – $0.05$ , and stellar ages from 1 Myr to 15 Gyr for a Chabrier initial mass function (IMF, Chabrier 2003). The best-fit stellar continuum was subtracted, and each emission line was subsequently fitted with a single Gaussian profile to generate the emission line maps. More details are provided in Lagos et al. (2022). Pixels and/or spaxels in the maps with a signal-to-noise ratio (S/N) of less than five were excluded from the analysis.

## 3. Results

### 3.1. H $\alpha$ emission line, EW(H $\alpha$ ), and $\sigma(H\alpha)$

Figure 1 shows our H $\alpha$  flux  $F(H\alpha)$ , H $\alpha$  equivalent width EW(H $\alpha$ ), and velocity dispersion  $\sigma(H\alpha)$  maps for UM 462 (upper panels) and IIZw40 (lower panels). We calculated  $\sigma(H\alpha)$  using the relation between velocity dispersion and full width at half maximum (FWHM),  $\sigma = \text{FWHM}/2.35$ , after correcting the measured FWHM for the instrumental broadening (FWHM<sub>inst</sub>  $\sim 2.6$  Å near H $\alpha$ ) and thermal broadening at  $10^4$  K. Our H $\alpha$  emission and EW(H $\alpha$ ) maps display similar morphologies to the H $\beta$  maps in Lagos et al. (2007), while the  $\sigma(H\alpha)$  maps resemble those shown by Monreal-Ibero et al. (2023) and Bordalo et al. (2009) for UM 462 and IIZw40, respectively, and they are also consistent with the maps presented by Marasco et al. (2023), who used the same dataset.

The  $F(H\alpha)$  maps for UM 462 and IIZw40 reveal a network of extended low-luminosity filamentary structures beyond the main HII regions tracing most of the DIG distribution. The EW(H $\alpha$ ) maps offer complementary information by measuring the relative strength of H $\alpha$  emission compared to the underlying stellar continuum. High EW values in the maps indicate the presence of

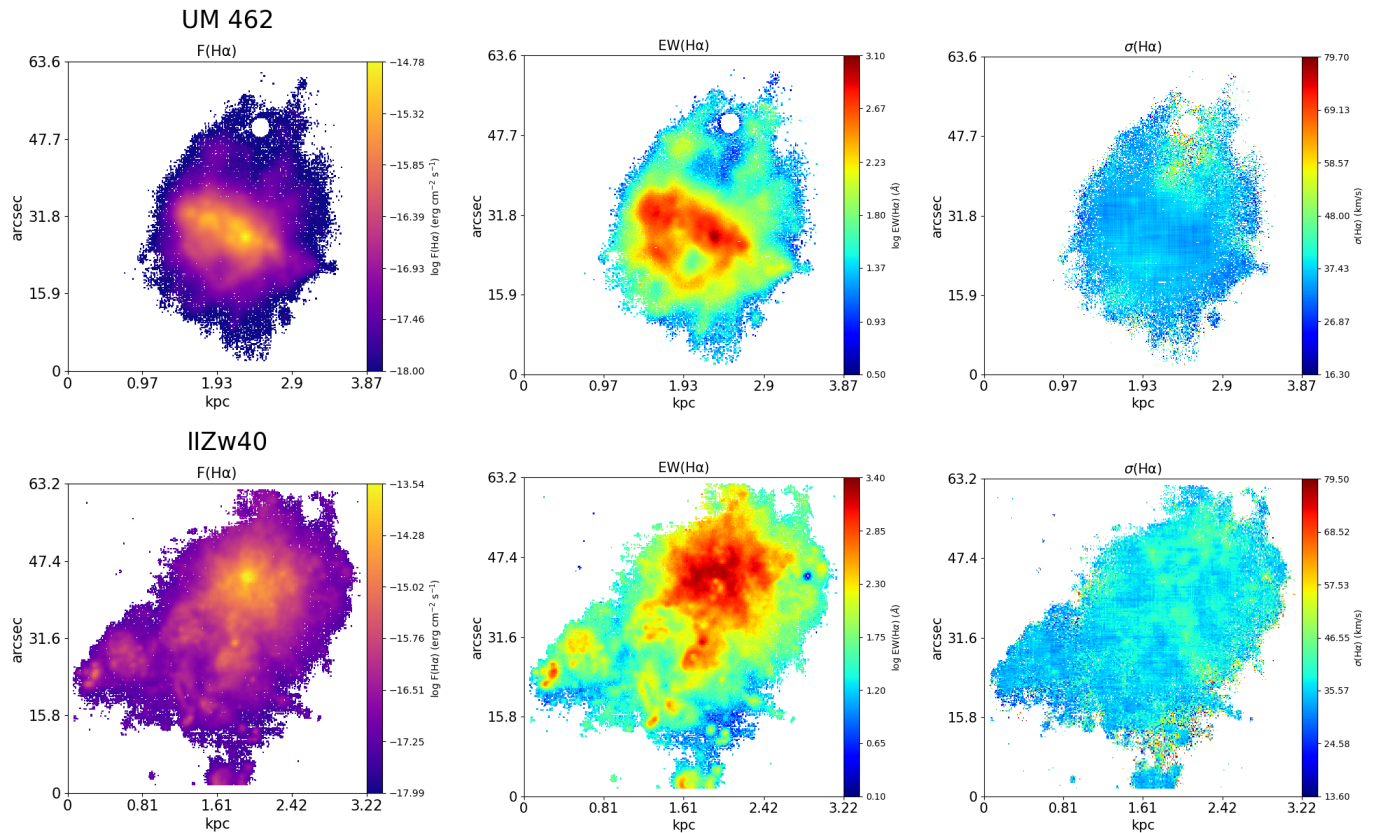


**Fig. 1.** F(H $\alpha$ ) maps (left panels), EW(H $\alpha$ ) maps (middle), and  $\sigma$ (H $\alpha$ ) maps (right). Pixels/spaxels with a S/N < 5 were removed. The colour scale at the right of each panel indicates the F(H $\alpha$ ), EW(H $\alpha$ ) and  $\sigma$ (H $\alpha$ ) levels, respectively. North is up and east is left.

young, massive star-forming regions, while lower values correspond to areas dominated by older stellar populations and DIG. In both galaxies, the EW distribution closely follows their morphological structure, highlighting the connection between star formation and the ionised gas environment. The velocity dispersion maps display a striking pattern, with the most kinematically disturbed regions located along filamentary structures and shells, or in cavities between these features. In both galaxies, these regions reach values  $\gtrsim 50$  km s $^{-1}$ . Those values are consistent with low-velocity shocks and line profile velocities of active galactic nuclei (AGNs) observed in high-redshift galaxies and/or star-forming clumps (e.g. Epinat et al. 2010; Elmegreen et al. 2007).

### 3.2. DIG definition and H $\alpha$ surface brightness ( $\Sigma$ (H $\alpha$ )) bins

Diffuse ionised gas is commonly defined using  $\Sigma$ (H $\alpha$ ) and/or EW(H $\alpha$ ). Zhang et al. (2017) defined the DIG-dominated regions as being those with  $\Sigma$ (H $\alpha$ )  $< 10^{39}$  erg s $^{-1}$  kpc $^{-2}$ . Using this definition, we found that 61% of the ionised gas is located in the HII-dominated regions of UM 462, and 39% is in the DIG-dominated regions. For IIIZw40, 93% of the ionised gas in the HII-dominated regions, and 7% is in the DIG-dominated regions. Using CALIFA data, Lacerda et al. (2018) classified DIG-dominated regions as those with EW(H $\alpha$ )  $< 3$  Å, while HII-dominated regions had EW(H $\alpha$ )  $> 14$  Å. Using this definition, only  $\sim 2\%$  of the data points, for both galaxies, have EW(H $\alpha$ )  $< 14$  Å, implying that several ionisation processes contribute to the DIG in UM 462 and IIIZw40. The ISM in low-mass galaxies is primarily photoionised by OB stars, but shock ionisation from star formation-driven feedback can extend over a large fraction

of the nebular region (Bordalo et al. 2009). Given that EW(H $\alpha$ ) is highly influenced by the local ISM conditions, the DIG will also be affected by the starburst energy injection. In galaxies with strong star formation, the DIG shows large EW(H $\alpha$ ) values (Lugo-Aranda et al. 2024). This is exactly what we find in our two studied galaxies. Figure 2 shows the histograms of  $\Sigma$ (H $\alpha$ ) and EW(H $\alpha$ ) for HII (red) and DIG-dominated (blue) spaxels for UM 462 and IIIZw40 using the  $\Sigma$ (H $\alpha$ ) definition of DIG.

In this study, we use the  $\Sigma$ (H $\alpha$ ) criterion of Zhang et al. (2017) to distinguish between HII- and DIG-dominated regions. To achieve this, we defined several regions within the galaxies grouped into different  $\log(\Sigma(\text{H}\alpha))$  bins. Figure 3 shows regions of the galaxies based on their  $\Sigma(\text{H}\alpha)$  bins  $37 - < 38$ ,  $38 - < 39$ ,  $39 - < 40$ ,  $40 - < 41$ ,  $41 - < 42$ , and  $42 - < 43$  in units of  $\log(\text{erg s}^{-1} \text{kpc}^{-2})$ . This figure highlights the more extended distribution of DIG in UM 462, which is reflected in its significantly higher fraction of DIG-dominated spaxels (as defined by  $\Sigma(\text{H}\alpha)$ ); see Fig. 2) compared to IIIZw40.

### 3.3. Emission line ratios

In Fig. 4 we show the  $\log([\text{OIII}]/\text{H}\beta)$ ,  $\log([\text{NII}]/\text{H}\alpha)$ , and  $\log([\text{SII}]/\text{H}\alpha)$  emission line ratios versus  $\log(\Sigma(\text{H}\alpha))$  for both galaxies. The vertical lines in this figure indicate the threshold distinguishing DIG-dominated regions when using the  $\Sigma(\text{H}\alpha)$  definition. We confirm that  $\log([\text{NII}]/\text{H}\alpha)$  and  $\log([\text{SII}]/\text{H}\alpha)$  emission line ratios are enhanced in the DIG regions, where we also find the lowest EW(H $\alpha$ ) values. In Fig. 5 we use those emission line ratios in conjunction with the Kewley et al. (2001) starburst and the Kauffmann et al. (2003) parameters to demarcate regions of OB-star-driven ionisation, mixed ionisation and AGN,

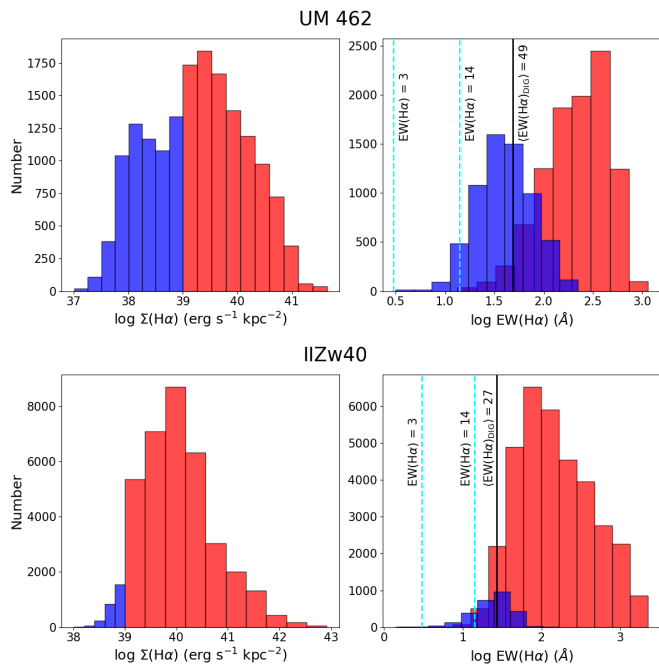


**Fig. 2.** Histograms of  $\Sigma(\text{H}\alpha)$  and  $\text{EW}(\text{H}\alpha)$ . The HII-dominated spaxel values are shown in red, while DIG-dominated spaxel values are in blue. The dotted cyan lines indicate the classification by Lacerda et al. (2018), where DIG-dominated regions have  $\text{EW}(\text{H}\alpha) < 3 \text{ \AA}$  and HII region-dominated areas have  $\text{EW}(\text{H}\alpha) > 14 \text{ \AA}$ . The mean spaxel values of our DIG-dominated areas are indicated by the vertical black lines.

shock or HOLMES ionisation in the classic Baldwin-Phillips-Terlevich (BPT; Baldwin et al. 1981) diagrams. Our results show that radiation from OB stars is likely the predominant ionisation source, with a smaller contribution from other sources in our galaxies. A significant fraction of the data points, mainly in the  $\log([\text{SII}]/\text{H}\alpha)$  versus  $\log([\text{OIII}]/\text{H}\beta)$  diagram, are above the boundary limits between HII and AGN/low-ionization nuclear emission-line regions (LINERs) in the BPT diagrams. This is most likely attributable to shock ionisation. We discuss this further in Sect. 4.

#### 3.4. Abundance determinations

To calculate the electron temperature, density, and oxygen abundances, in the HII-dominated pixels and/or spaxels we used the PyNEB package (Luridiana et al. 2015), version 1.1.13, with the default set of atomic data (transition probabilities and collision cross-sections). We used `S2.getTemDen()`, ‘L(6717) / L(6731)’, and  $T_e = 10^4 \text{ K}$  for the  $n_e$ , while the  $T_e([\text{SIII}])$  was determined using `S3.getTemDen()`, ‘L(6312) / L(9069)’, and the previously determined  $n_e$ . Ionic abundances were calculated using the `Atom.getTemDen()` method and the emission lines  $[\text{OIII}]\lambda\lambda 4959, 5007$  and  $[\text{OII}]\lambda\lambda 7320, 7331$  for the determination of  $\text{O}^+/\text{H}^+$  and  $\text{O}^{++}/\text{H}^+$ , respectively. We considered the total oxygen abundance as  $\text{O/H} = \text{O}^+/\text{H}^+ + \text{O}^{++}/\text{H}^+$ . Our spatially resolved results, in the case of UM 462, are similar to those from Montreal-Ibero et al. (2023), indicating we achieved reliable and consistent results for both galaxies. We found a mean  $12 + \log(\text{O/H})$  of 8.01 and 8.0 with a standard deviation of 0.22 dex and 0.32 dex for UM 462 and IIIZw40, respectively. Those results are consistent with the integrated values of 8.02 and 8.07 found by Montreal-Ibero et al. (2023) and Bordalo & Telles (2011) for UM 462 and IIIZw40, respectively. Addition-

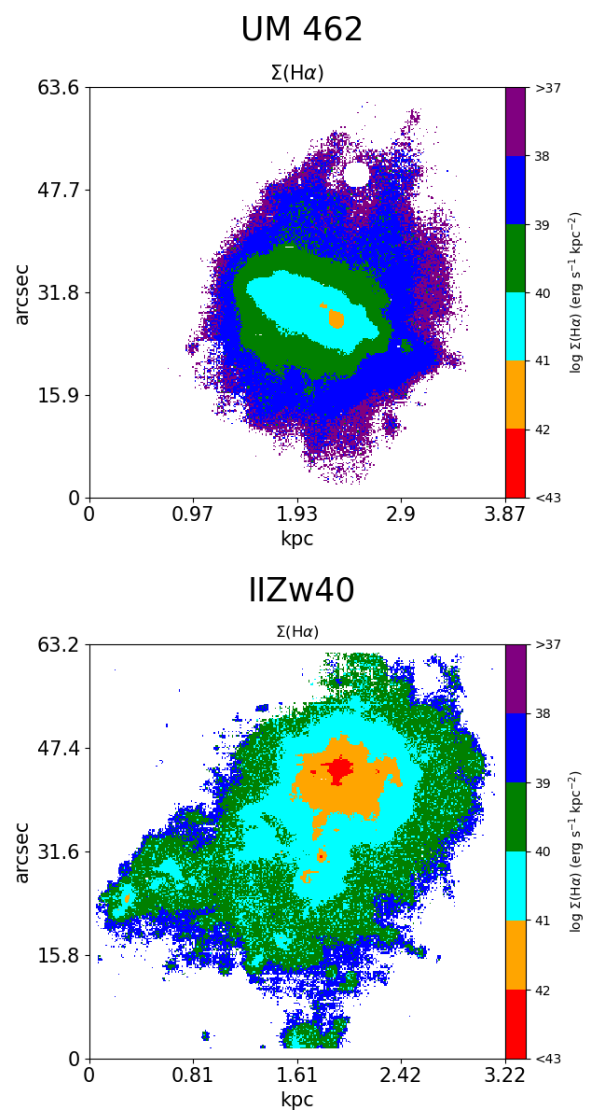


**Fig. 3.**  $\text{H}\alpha$  Surface brightness maps. The colour-code represents the regions of the galaxies divided into different  $\Sigma(\text{H}\alpha)$  bins of  $37-38$  (purple),  $38-39$  (blue),  $39-40$  (green),  $40-41$  (cyan),  $41-42$  (orange), and  $42-43$  (red) in units of  $\log \text{erg s}^{-1} \text{ kpc}^{-2}$ . North is up, and east is left.

ally, we determined the oxygen abundances using the indices  $\text{N2} = \log([\text{NII}]\lambda 6584/\text{H}\alpha)$  and  $\text{O3N2} = \log([\text{OIII}]\lambda 5007/\text{H}\beta \times \text{H}\alpha/[\text{NII}]\lambda 6584)$ , together with the calibrators from Denicoló et al. (2002) (D), Pettini & Pagel (2004) (PP), and Marino et al. (2013) (M). The  $\text{O/H}$  abundances in the different  $\Sigma(\text{H}\alpha)$  bins were derived using the HII-based methods described above after removing the data points above the Kauffmann et al. (2003) demarcation (dashed line in Fig. 5) in order to exclude regions ionised by sources other than young stars in HII regions. Figure 6 shows the oxygen abundance versus distance (in kiloparsecs) from the  $\text{H}\alpha$  maxima for all spaxels (left panels) and those classified as DIG (right panels). Figure 7 presents the same relation, divided into  $\Sigma(\text{H}\alpha)$  bins, with each panel showing results from different calibrators and the direct method. In Table 2 we present the mean and standard deviation of the  $12 + \log(\text{O/H})$  values for all data points as well as for those with  $\Sigma(\text{H}\alpha) < 39$  (DIG-dominated). In Table 3, we show the same quantities but computed across the  $\Sigma(\text{H}\alpha)$  bins defined in this study. This table also presents the  $\text{EW}(\text{H}\alpha)$ , the ionisation parameter (discussed

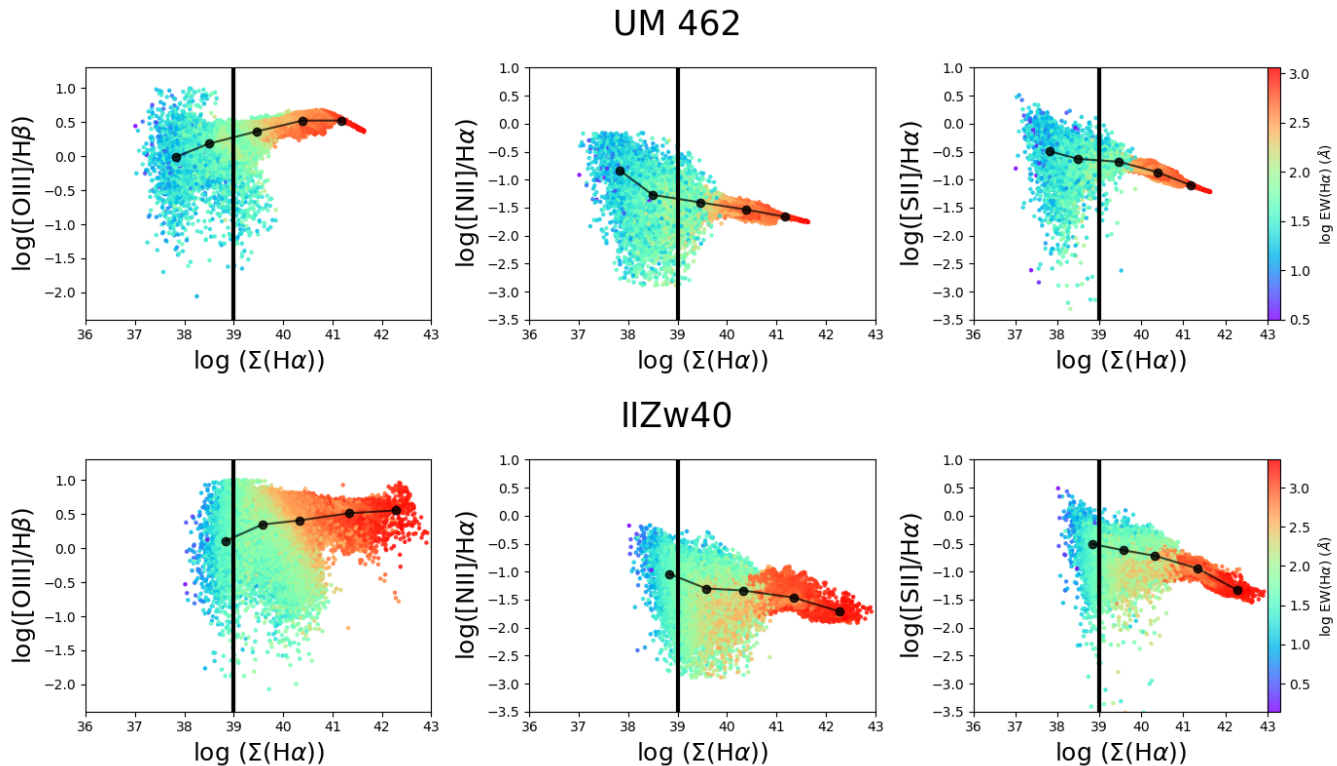


**Fig. 4.** Emission line ratios  $\log([OIII]\lambda 5007/H\beta)$ ,  $\log([SII]\lambda\lambda 6717,6731/H\alpha)$ , and  $\log([NII]\lambda 6584/H\alpha)$  versus  $\log(\Sigma(H\alpha))$ . The vertical line indicates the threshold distinguishing DIG-dominated regions, defined as areas with  $\Sigma(H\alpha) < 10^{39} \text{ erg s}^{-1} \text{ kpc}^{-2}$ . The black data points correspond to the mean values within the different  $\Sigma(H\alpha)$  bins defined in Sect. 3.2. There is a clear increasing pattern of  $[SII]/H\alpha$  and  $[NII]/H\alpha$  ratios and a decreasing trend of  $[OIII]/H\beta$  as  $\Sigma(H\alpha)$  decreases. The colour scale at the right of each panel indicates the  $\log(EW(H\alpha))$ .

in Sect. 4), and the  $\sigma(H\alpha)$  values for the different  $\Sigma(H\alpha)$  bins. We observed a clear increase in the mean metallicity values with decreasing  $\Sigma(H\alpha)$  when using both the N2 and O3N2 indices and all calibrators (see Figs. 6 and 7). An increasing trend in  $12 + \log(O/H)$  was also observed when using the direct method in the HII-dominated regions. However, the difference is not statistically significant within the uncertainties.

#### 4. Discussion and conclusions

We now examine how the oxygen abundance and related ionisation properties vary with  $H\alpha$  surface brightness across the galaxies. In Fig. 8 we present, for each galaxy, the mean  $12 + \log(O/H)$  derived from the calibrators across the  $\Sigma(H\alpha)$  bins. The colour scale on the right gives the mean  $EW(H\alpha)$  of each bin. The left inset panels show the ionisation parameter  $U$  (the relative number of ionising photons compared to the number of hydrogen atoms) as a function of  $EW(H\alpha)$ . The right inset panels show the deviation of the oxygen abundance ( $\Delta(O/H)$ ) derived using the calibrators from the mean  $O/H$  value as a function of  $EW(H\alpha)$  for the same  $\Sigma(H\alpha)$  bins. This figure reveals a notable correlation between high metallicity and regions of low  $\Sigma(H\alpha)$ .

Historically, the mean  $12 + \log(O/H)$  value has been considered as a reliable representation of the overall ISM chemical composition. For most HII or BCD galaxies reported in the literature – including those in this study – the evidence (see Lagos et al. 2009, 2012; Lagos & Papaderos 2013) suggests that they are chemically homogeneous when using the HII-based methods. Using the strong-line calibrators (see Fig. 8), regions with the lowest  $\Sigma(H\alpha)$  exhibit  $12 + \log(O/H)$  values higher than the mean by  $\sim 0.2$  dex in UM 462 and  $\sim 0.1$  dex in IIIZw40. In con-

**Table 2.** Mean and standard deviation of  $12 + \log(O/H)$  for all and  $\Sigma(H\alpha) < 39$  (DIG-dominated) data points. Values were derived using the direct method (DM)  $T_e([SIII])$  and the N2 and O3N2 calibrators from Denicoló et al. (2002) (D), Pettini & Pagel (2004) (PP), and Marino et al. (2013) (M).

Method	12 + $\log(O/H)$	
	UM 462	IIIZw 40
All data points		
DM $T_e([SIII])$	$8.01 \pm 0.22$	$8.00 \pm 0.33$
N2 D	$8.12 \pm 0.25$	$8.14 \pm 0.20$
O3N2 PP	$8.20 \pm 0.17$	$8.20 \pm 0.15$
N2 PP	$8.12 \pm 0.19$	$8.14 \pm 0.15$
O3N2 M	$8.18 \pm 0.11$	$8.18 \pm 0.10$
N2 M	$8.11 \pm 0.16$	$8.13 \pm 0.13$
Data points with $\log \Sigma(H\alpha) < 39$ (DIG)		
DM $T_e([SIII])$	...	...
N2 D	$8.24 \pm 0.33$	$8.34 \pm 0.29$
O3N2 PP	$8.31 \pm 0.19$	$8.31 \pm 0.21$
N2 PP	$8.21 \pm 0.26$	$8.29 \pm 0.23$
O3N2 M	$8.25 \pm 0.13$	$8.25 \pm 0.14$
N2 M	$8.18 \pm 0.21$	$8.25 \pm 0.19$

**Notes.** Values are given as mean  $\pm$  standard deviation.

trast, metallicity differences reach about 0.4 dex and 0.3 dex between the highest and lowest  $\Sigma(H\alpha)$  bins in UM 462 and IIIZw40, respectively. These results indicate that significant O/H variations are observed in the DIG-dominated regions (see Figs. 6 and 7) compared to the HII-dominated ones, based on both the direct

**Table 3.** Mean and standard deviation of 12+log(O/H) for the  $\Sigma(\text{H}\alpha)$  bins. The values were derived using the direct method (DM)  $T_e(\text{[SIII]})$  and the N2 and O3N2 calibrators from Denicoló et al. (2002) (D), Pettini & Pagel (2004) (PP), and Marino et al. (2013) (M).

log( $\Sigma(\text{H}\alpha)$ )	37-<38	38-<39	39-<40	40-<41	41-<42	42-<43	12 + log(O/H)
<i>UM 462</i>							
DM $T_e(\text{[SIII]})$	...	...	...	$8.02 \pm 0.22$	$7.98 \pm 0.08$	...	
N2 D	$8.39 \pm 0.31$	$8.17 \pm 0.29$	$8.09 \pm 0.13$	$8.00 \pm 0.06$	$7.90 \pm 0.03$	...	
O3N2 PP	$8.44 \pm 0.20$	$8.27 \pm 0.16$	$8.18 \pm 0.10$	$8.07 \pm 0.04$	$8.03 \pm 0.01$	...	
N2 PP	$8.33 \pm 0.25$	$8.16 \pm 0.22$	$8.09 \pm 0.10$	$8.02 \pm 0.05$	$7.95 \pm 0.02$	...	
O3N2 M	$8.34 \pm 0.13$	$8.23 \pm 0.11$	$8.16 \pm 0.07$	$8.09 \pm 0.03$	$8.07 \pm 0.01$	...	
N2 M	$8.28 \pm 0.20$	$8.14 \pm 0.18$	$8.09 \pm 0.10$	$8.02 \pm 0.05$	$7.95 \pm 0.02$	...	
log(EW(H $\alpha$ ))	$1.37 \pm 0.22$	$1.67 \pm 0.25$	$2.18 \pm 0.29$	$2.57 \pm 0.16$	$2.88 \pm 0.09$	...	
log(U)	$-3.18 \pm 0.77$	$-2.98 \pm 0.54$	$-3.0 \pm 0.16$	$-2.68 \pm 0.16$	$-2.3 \pm 0.10$	...	
log( $\sigma(\text{H}\alpha)$ )	$1.55 \pm 1.00$	$1.57 \pm 0.73$	$1.56 \pm 0.32$	$1.55 \pm 0.03$	$1.54 \pm 0.00$	...	
<i>IIZw 40</i>							
DM $T_e(\text{[SIII]})$	...	...	...	$8.08 \pm 0.38$	$7.94 \pm 0.24$	$7.80 \pm 0.21$	
N2 D	...	$8.29 \pm 0.29$	$8.15 \pm 0.21$	$8.13 \pm 0.14$	$8.05 \pm 0.11$	$7.88 \pm 0.09$	
O3N2 PP	...	$8.34 \pm 0.19$	$8.21 \pm 0.15$	$8.20 \pm 0.13$	$8.11 \pm 0.07$	$8.03 \pm 0.10$	
N2 PP	...	$8.26 \pm 0.23$	$8.14 \pm 0.17$	$8.12 \pm 0.11$	$8.07 \pm 0.09$	$7.93 \pm 0.07$	
O3N2 M	...	$8.27 \pm 0.13$	$8.18 \pm 0.10$	$8.18 \pm 0.09$	$8.12 \pm 0.05$	$8.06 \pm 0.06$	
N2 M	...	$8.22 \pm 0.18$	$8.13 \pm 0.13$	$8.12 \pm 0.11$	$8.07 \pm 0.09$	$7.93 \pm 0.07$	
log(EW(H $\alpha$ ))	...	$1.37 \pm 0.24$	$1.86 \pm 0.30$	$2.34 \pm 0.36$	$2.96 \pm 0.18$	$3.14 \pm 0.18$	
log(U)	...	$-3.2 \pm 0.61$	$-3.06 \pm 0.35$	$-2.92 \pm 0.24$	$-2.52 \pm 0.22$	$-1.94 \pm 0.19$	
log( $\sigma(\text{H}\alpha)$ )	...	$1.57 \pm 0.98$	$1.56 \pm 0.56$	$1.57 \pm 0.43$	$1.57 \pm 0.32$	$1.58 \pm 0.30$	

**Notes.** Values are given as mean  $\pm$  standard deviation. Mean values of log(EW(H $\alpha$ )) (Å), log(U) and log( $\sigma(\text{H}\alpha)$ ) (km s $^{-1}$ ) are also reported in the corresponding  $\Sigma(\text{H}\alpha)$  bins.

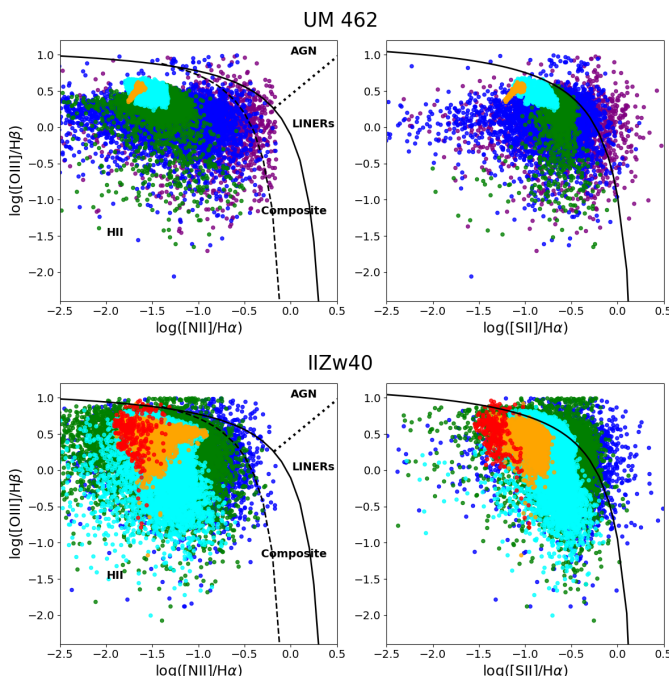


**Fig. 5.** BPT diagrams  $\log([\text{OIII}]/\text{H}\beta)$  versus  $\log([\text{NII}]/\text{H}\alpha)$  and  $\log([\text{OIII}]/\text{H}\beta)$  versus  $\log([\text{SII}]/\text{H}\alpha)$  for UM 462 (upper panels) and IIZw40 (lower panels). The colour code represents the spaxels of the galaxies divided into the different  $\log(\Sigma(\text{H}\alpha))$  bins of  $<38-37$  (purple),  $<39-38$  (blue),  $<40-39$  (green),  $<41-40$  (cyan),  $<42-41$  (orange), and  $<43-42$  (red) in units of  $\log \text{erg s}^{-1} \text{kpc}^{-2}$ . In the BPT diagrams, we include the Kewley et al. (2001) (solid lines), Kauffmann et al. (2003) (dashed lines), and Schawinski et al. (2007) (dotted lines) model boundary lines, which divide regions dominated by star-forming HII, composite, and AGN/LINERs.

method and strong-line calibrators, although the overall chemical composition appears homogeneous within the uncertainties.

Despite the scatter in the outer low surface brightness regions in Fig. 5, there is a clear increase in the emission line ratios [NII]/H $\alpha$  and [SII]/H $\alpha$ , and consequently in metallicity, from the centre outwards, indicating a physically meaningful gradient. The metallicity derived using N2 and/or O3N2 at large radii ( $\Sigma(\text{H}\alpha)$  bins 37 - <38 and 38 - <39 in units of  $\log \text{erg s}^{-1} \text{kpc}^{-2}$ ) are ionised by several different sources (e.g. photon leaked from the HII regions and/or HOLMES) rather than young massive stars within HII regions. According to Belfiore et al. (2022), the increase in [NII]/H $\alpha$  and [SII]/H $\alpha$  ratios along with a decrease in [OIII]/H $\beta$  ratios can be explained by DIG ionisation driven primarily by leaking radiation from HII regions, with a minor contribution from HOLMES. This may account for the observed increase in emission line ratios as a function of  $\Sigma(\text{H}\alpha)$  in Fig. 4.

Using the [SII] $\lambda\lambda 6717,6731/\text{H}\alpha$  emission line ratios in Sect. 3.3 and the parametrisation by Dors et al. (2011), we calculated the ionisation parameter U (see insets in Fig. 8). In Table 3 we show the mean and standard deviation of log(U) values across the different  $\Sigma(\text{H}\alpha)$  bins. In both galaxies, the metallicity (from the calibrators) relative to the mean shows a linear correlation with log EW(H $\alpha$ ) (see Fig. 8, blue lines, right insets). Moreover, log(U) in the HII-dominated regions is also correlated with EW(H $\alpha$ ) (Fig. 8 left insets, red lines) at least for UM 462. A similar relation between log(U) and log(EW(H $\alpha$ )) was seen in Mingozi et al. (2020). However, when both HII and DIG-dominated regions are included, the relation follows a power-law (Fig. 8, left insets, blue lines) of the form  $\log(U) \propto \log(\text{EW}(\text{H}\alpha))^\alpha$ , where  $\alpha$  should be a characteristic constant of each galaxy. For UM 462 and IIZw40  $\alpha = 5.76$  and  $9.89$ , respectively. These relationships reveal a continuous and smooth variation in the ionisation structure from the central HII regions into the low surface brightness regions, with a declining EW(H $\alpha$ ) and an increasing

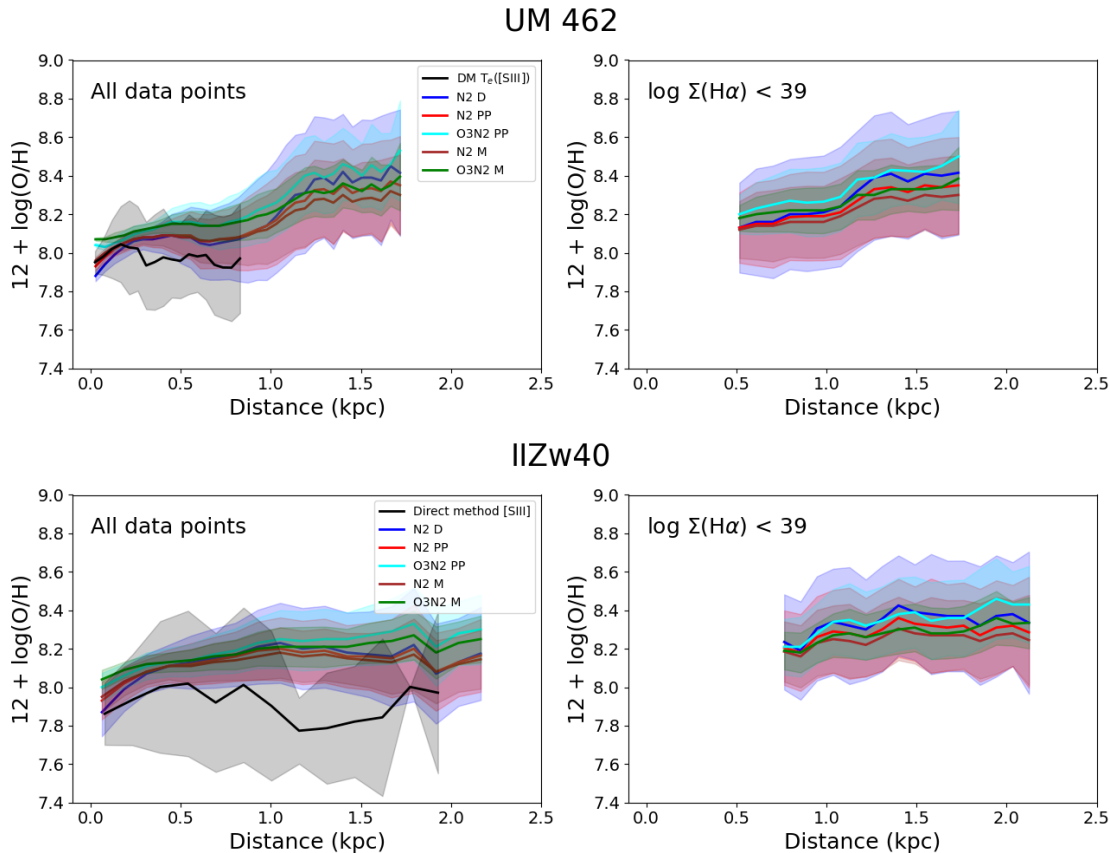


**Fig. 6.** Mean  $12 + \log(\text{O/H})$  profiles for all data points (left panels) and those with  $\log \Sigma(\text{H}\alpha) < 39$  in units of  $\log \text{erg s}^{-1} \text{kpc}^{-2}$  (right panels) derived using the direct method  $T_e(\text{[SIII]})$  and the N2 and O3N2 strong-line calibrators from Denicoló et al. (2002) (D), Pettini & Pagel (2004) (PP), and Marino et al. (2013) (M). The standard deviation of the  $12 + \log(\text{O/H})$  values are indicated by the shaded regions. A clear increase in mean metallicity is observed with distance when using all HII-based calibrators as well as the N2 and O3N2 indices for both the full dataset and the subset with  $\log \Sigma(\text{H}\alpha) < 39$ . When applying the direct method, the metallicity distribution across the ISM appears flat.

O/H (see Fig. 8), when using the N2- and O3N2-based calibrators. This suggests that the DIG emission is primarily maintained by ionising photons escaping from the HII regions (McClintock et al. 2024) through a porous or leaky ISM.

In Fig. 9 for each galaxy we show  $\log(\text{EW}(\text{H}\alpha))$  versus  $\log(\sigma(\text{H}\alpha))$  across the  $\Sigma(\text{H}\alpha)$  bins. Sánchez et al. (2024) used this diagram (WHD diagram) to separate galaxies and/or regions dominated by star-forming galaxies, retired galaxies (HOLMES or post-AGBs), AGNs and weak AGNs. The shape of this diagram resembles the intensity-velocity dispersion (I- $\sigma$ ) relation of emission lines, which is commonly used to study giant HII regions and HII or BCD galaxies (Bordalo et al. 2009; Martínez-Delgado et al. 2007; Moiseev & Lozinskaya 2012, and references therein). This approach, represented in the Sánchez et al. (2024) diagram, is well suited to identifying the kinematic features of our studied galaxies. In our case, most data points are clearly located in the HII-dominated areas, with  $\text{EW}(\text{H}\alpha) > 14 \text{ \AA}$  (Lacerda et al. 2018). The central and vertical bands in Fig. 9 correspond to the HII-dominated regions, with the bulk of  $\sigma(\text{H}\alpha)$  values ranging from  $\sim 30$  to  $\sim 44 \text{ km s}^{-1}$  in UM 462 and from  $\sim 25$  to  $\sim 52 \text{ km s}^{-1}$  in IIIZw40. In contrast, the more extended and disturbed bands, with  $\sigma(\text{H}\alpha)$  values ranging from  $\sim 16$  to  $\sim 80 \text{ km s}^{-1}$  in UM 462 and from  $\sim 20$  to  $\sim 80 \text{ km s}^{-1}$  in IIIZw40, are associated with the DIG-dominated regions. These DIG regions exhibit broader and more asymmetric line profiles (see Bordalo et al. 2009; Monreal-Ibero et al. 2023), produced by the impact of stellar mechanical energy on the ISM due to multiple massive

star-formation regions, which are often observed in BCD galaxies (e.g. Lagos et al. 2011). In our systems, stellar feedback is manifested in large-scale super-bubbles and/or shells (Monreal-Ibero et al. 2023; Bordalo et al. 2009). For instance, in UM 462, the horn-like DIG structures in the northern part of the galaxy are interpreted by Monreal-Ibero et al. (2023) as fragmented walls of a super-bubble, which may provide channels for ionising photons to escape. In any case,  $\sigma(\text{H}\alpha)$  values exceeding  $\sim 57 \text{ km s}^{-1}$  ( $\sim 1.76$  in log; the boundary in the WHD diagram that separates HII from AGN-like regions) indicate clear shock contamination in some parts of the DIG (also see Fig. 5 in Marasco et al. 2023). Consequently, such contamination may affect the reliability of the derived oxygen abundances in those regions.

High  $\text{EW}(\text{H}\alpha)$  values are typically associated with intense recent star-formation episodes, as they trace regions dominated by young massive stars. However, our DIG-dominated regions show relatively high  $\text{EW}(\text{H}\alpha)$  values, although still lower than those found in the HII-dominated regions, with a mean of  $49 \text{ \AA}$  and  $27 \text{ \AA}$  for UM 462 and IIIZw40, respectively. As discussed by Sánchez (2020) and Lugo-Aranda et al. (2024), the dominant ionising source of the DIG varies with galaxy morphological type. In early-type galaxies, a few HII regions together with older stellar populations provide potential DIG ionising sources, including HOLMES or post-AGB stars, and low-velocity shocks, with the latter typically playing a minor role. In contrast, in later-type galaxies, ionisation by leaking photons from a large number of HII regions may account for a large

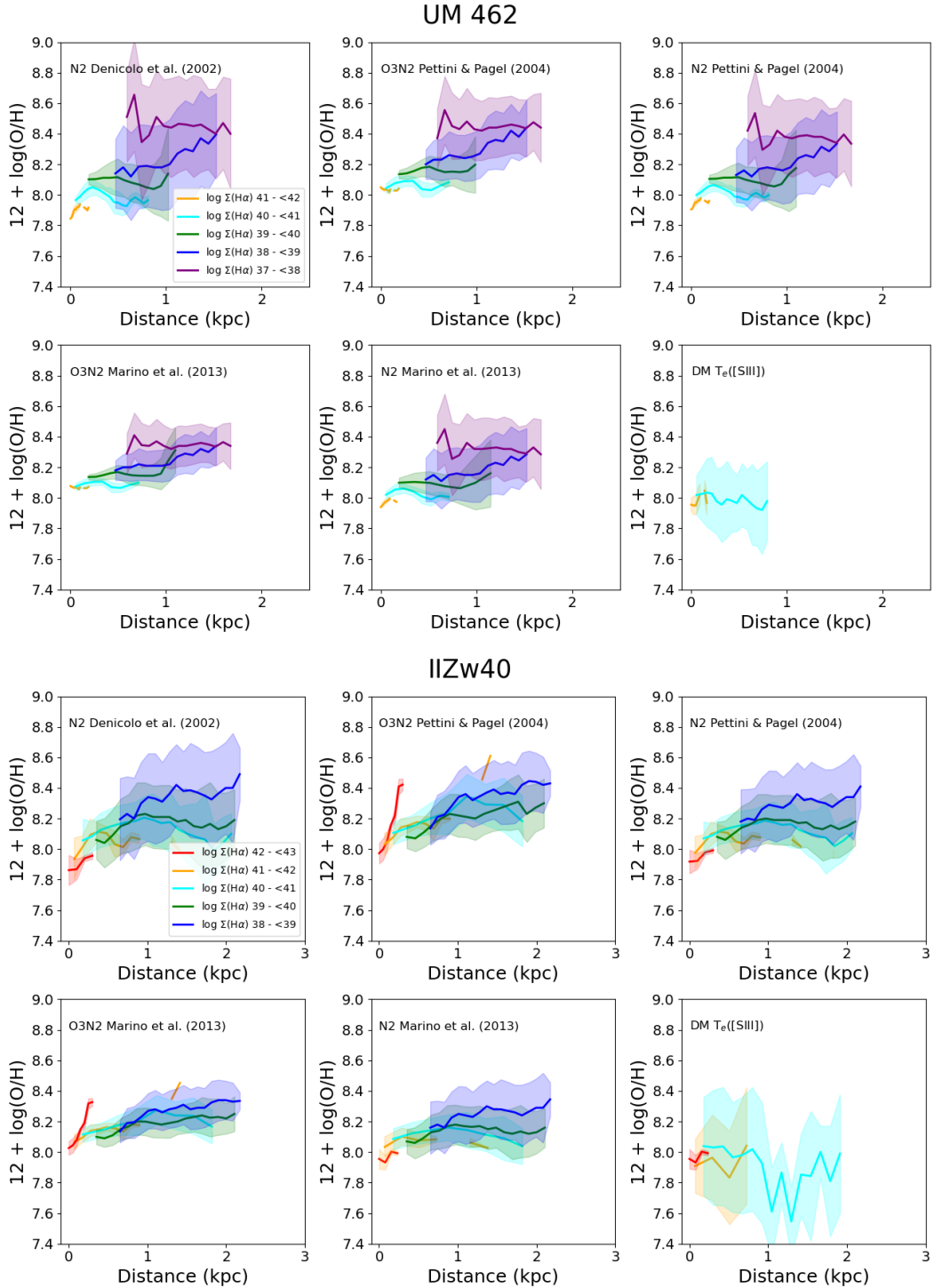


**Fig. 7.** Mean  $12 + \log(O/H)$  profiles for levels of  $\Sigma(H\alpha)$  for UM 462 (upper panels) and IIIZw40 (lower panels). The standard deviation for the different  $12 + \log(O/H)$  values within each bin are indicated by the shaded regions. A clear increase in the mean metallicity values can be observed with decreasing  $\Sigma(H\alpha)$  when using both the N2 and O3N2 indices across all calibrators. A slight upwards trend in  $12 + \log(O/H)$  is also observed with the direct method in the HII-dominated regions. However, this difference is not statistically significant within the uncertainties.

fraction of the DIG emission. Consequently, in areas near HII regions, the DIG is most likely dominated by leaked radiation and shocks (e.g. González-Díaz et al. 2024), resulting in a more kinematically disturbed ISM (Levy et al. 2019). The  $EW(H\alpha)$  in these regions is expected to be higher than in those dominated by HOLMES-like ionising sources (Lugo-Aranda et al. 2024). This is exactly what our results indicate.

Regardless of the main mechanism responsible for ionising the DIG, it is important to bear in mind that strong-line metallicity calibrators are typically obtained from HII-regions, which introduce biases when considering emission from the DIG. The metallicity gradients observed in star-forming galaxies are interpreted as signatures of several chemical enrichment processes, including stellar feedback, galactic outflows and fountains, inflows of metal-poor gas, mergers, and tidal interactions. As a

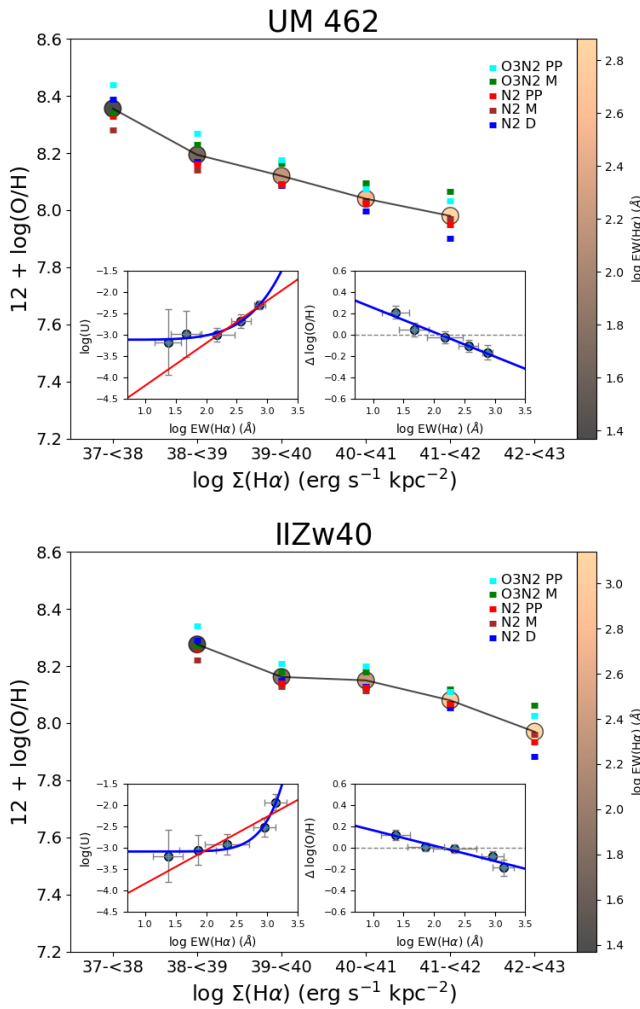


**Fig. 8.** Relationship between the mean  $12 + \log(\text{O/H})$  and surface brightness bins for UM 462 and IIIZw40. The values from the calibrators used in this study are indicated by the coloured squares in the figure. The inset panels show the  $\log(U)$  (left panels) and the difference in O/H relative to the mean value of the galaxies ( $\Delta(\text{O/H})$ ; right panels) as functions of the  $\text{EW}(\text{H}\alpha)$ . Oxygen abundances show an inverse correlation with  $\Sigma(\text{H}\alpha)$ . The DIG-dominated regions exhibit the highest oxygen abundances together with the lowest ionisation parameters and  $\text{EW}(\text{H}\alpha)$  values. We found a linear correlation between  $\Delta(\text{O/H})$  and  $\text{EW}(\text{H}\alpha)$ .

result of these mechanisms, star-forming galaxies with stellar masses of  $M_\star > 10^{9.5} M_\odot$  typically exhibit a well-defined oxygen abundance gradient of about -0.1 dex/Re across their discs, with local deviations such as central drops and outer flattening linked to gas flows and mixing (Sánchez et al. 2014; Sánchez 2020). In contrast, low-mass systems, ( $M_\star < 10^9 M_\odot$ ) including HII or BCD galaxies, are largely chemically homogeneous on galactic scales. The fact that we find chemical homogeneity in HII-dominated regions using the direct method suggests that metals in the ISM are distributed ‘globally’ throughout the ISM of the galaxies on a relatively short timescale (Lagos et al. 2016). Moreover, the strong-line N2- and O3N2-based calibrators in Figs. 6 and 7 show an increasing abundance pattern that is more pronounced in DIG-dominated areas. These results can be extrapolated to galaxies with extended DIG tails, such as tadpole or cometary-like systems, where previous studies (e.g. Sánchez Almeida et al. 2015) have suggested the presence of metallicity gradients. Such variations, however, can be misinterpreted as

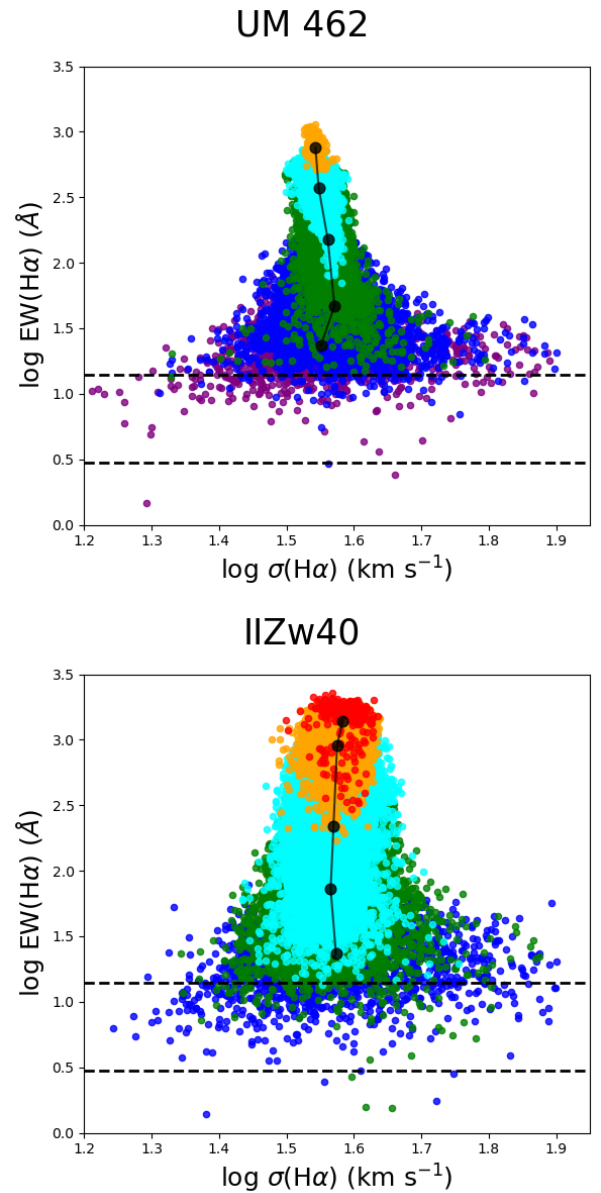


**Fig. 9.** Resolved  $\log(\text{EW}(\text{H}\beta))$  versus  $\log(\sigma(\text{H}\alpha))$  for UM 462 (upper panel) and IIIZw40 (lower panel). The colour code represents the regions of the galaxies divided into different  $\Sigma(\text{H}\alpha)$  bins of  $37 - < 38$  (purple),  $38 - < 39$  (blue),  $39 - < 40$  (green),  $40 - < 41$  (cyan),  $41 - < 42$  (orange), and  $42 - < 43$  (red) in units of  $\log \text{erg s}^{-1} \text{kpc}^{-2}$ . The dotted horizontal lines indicate the classification proposed by Lacerda et al. (2018), where HOLMES DIG-dominated regions have  $\text{EW}(\text{H}\alpha) < 3 \text{ \AA}$  (lower dashed line), and HII-dominated areas have  $\text{EW}(\text{H}\alpha) > 14 \text{ \AA}$  (upper dashed line). The black data points correspond to the mean values within the different  $\Sigma(\text{H}\alpha)$  bins. The central and vertical bands clearly correspond to the HII-dominated regions, whereas the more disturbed, extended bands are those associated with the DIG-dominated areas.

evidence of the infall of metal-poor gas. Because DIG regions are characterised by physical conditions that differ from those in HII regions, such as different ionisation sources, lower ionisation parameters, and a more extended spatial distribution, they can produce artificially inverted metallicity gradients if not properly accounted for.

Although derivations using HII-based methods may help estimate the level of DIG contamination, they do not trace real changes in metallicity but rather apparent variations caused by

differing ionisation sources. Again, it is also important to note that the N2 and O3N2 calibrations are tuned for classical HII regions, not for DIG. The N2 index depends on the [NII]/H $\alpha$  ratio, and since nitrogen is a secondary nucleosynthesis product, its abundance can vary with the star-formation history (i.e. with N/O; Izotov & Thuan 1999; Izotov et al. 2006). Moreover, both N2 and O3N2 are sensitive to changes in  $U$ . These limitations introduce unquantified uncertainties into the separation of HII and DIG regions and their interpretation. In BCD galaxies with complex morphologies (featuring optically thin media that allow enhanced LyC photon leakage and significant DIG fractions), the interpretation of metallicity gradients based on strong-line calibrators must account for these structural effects to avoid misleading conclusions about chemical evolution. If our interpretation is correct, similar issues should also be observable in other local low-mass systems, such as HII or BCD galaxies and XMPs as well as in Green Pea galaxies at intermediate redshift and in high-redshift star-forming galaxies and clumps.

According to Mannucci et al. (2021), the differences between the spectra of local HII regions and more distant galaxies are not caused by contamination from the DIG but by an aperture effect. However, we expect aperture effects to further amplify this bias, as integrated spectra based on larger apertures tend to include a greater fraction of DIG emission, which is preferentially located in the outer parts of the galaxies (see Fig. 3). In strong starbursts such as IIZw40, the DIG emission is difficult to separate from the HII-dominated regions, making DIG contamination harder to resolve. The difference in the distribution and amount of DIG in the two galaxies appears to be influenced by their distinct evolutionary states: IIZw40 is in the midst of a merger, whereas UM 462, although part of a small group together with UM 461 (Lagos et al. 2018), presents as a relatively undisturbed galaxy. These findings indicate that the interplay between star formation, gas dynamics, and environment play a crucial role in shaping the properties of the diffuse ionised medium. Therefore, we conclude that the most likely mechanism for ionising the DIG in our sample of local analogues of high-redshift star-forming galaxies (HII or BCD galaxies) is the leakage of photons from HII regions, with shocks induced in the ISM by feedback processes also acting as an important ionisation source.

Finally, our results highlight the importance of accounting for DIG and aperture effects when interpreting metallicities, particularly in distant galaxies, where data may be limited to integrated values. Even in the local Universe, spatially resolved studies based on strong-line calibrators may be affected by uncorrected DIG contamination, thus potentially biasing metallicity gradient measurements.

**Acknowledgements.** We thank the referee for his/her careful reading of the manuscript and helpful comments which substantially improved the paper. PL gratefully acknowledges support by the GEMINI ANID project No. 32240002. PL (10.54499/DL57/2016/CP1364/CT0010) and TS (10.54499/DL57/2016/CP1364/CT0009) are supported by national funds through FCT and CAUP. RD gratefully acknowledges support by the ANID BASAL project FB210003.

Belfiore, F., Santoro, F., Groves, B., et al. 2022, A&A, 659, A26  
 Binette, L., Flores-Fajardo, N., Raga, A. C., Drissen, L., & Morisset, C. 2009, ApJ, 695, 552  
 Bordalo, V., Plana, H., & Telles, E. 2009, ApJ, 696, 1668  
 Bordalo, V. & Telles, E. 2011, ApJ, 735, 52  
 Bruzual, G. & Charlot, S. 2003, MNRAS, 344, 1000  
 Cardelli, J. A., Clayton, G. C., & Mathis, J. S. 1989, ApJ, 345, 245  
 Chabrier, G. 2003, PASP, 115, 763  
 Denicoló, G., Terlevich, R., & Terlevich, E. 2002, MNRAS, 330, 69  
 Dopita, M. A. & Sutherland, R. S. 1995, ApJ, 455, 468  
 Dors, Jr., O. L., Krabbe, A., Hägele, G. F., & Pérez-Montero, E. 2011, MNRAS, 415, 3616  
 Elmegreen, D. M., Elmegreen, B. G., Ravindranath, S., & Coe, D. A. 2007, ApJ, 658, 763  
 Epinat, B., Amram, P., Balkowski, C., & Marcelin, M. 2010, MNRAS, 401, 2113  
 Giammanco, C., Beckman, J. E., Zurita, A., & Relaño, M. 2004, A&A, 424, 877  
 Gomes, J. M. & Papaderos, P. 2017, A&A, 603, A63  
 González-Díaz, R., Rosales-Ortega, F. F., & Galbany, L. 2024, A&A, 691, A25  
 Izotov, Y. I., Stasińska, G., Meynet, G., Guseva, N. G., & Thuan, T. X. 2006, A&A, 448, 955  
 Izotov, Y. I. & Thuan, T. X. 1999, ApJ, 511, 639  
 Kaplan, K. F., Jogee, S., Kewley, L., et al. 2016, MNRAS, 462, 1642  
 Kauffmann, G., Heckman, T. M., Tremonti, C., et al. 2003, MNRAS, 346, 1055  
 Kewley, L. J. & Dopita, M. A. 2002, ApJS, 142, 35  
 Kewley, L. J., Dopita, M. A., Sutherland, R. S., Heisler, C. A., & Trevena, J. 2001, ApJ, 556, 121  
 Lacerda, E. A. D., Cid Fernandes, R., Couto, G. S., et al. 2018, MNRAS, 474, 3727  
 Lagos, P., Demarco, R., Papaderos, P., et al. 2016, MNRAS, 456, 1549  
 Lagos, P., Loubser, S. I., Scott, T. C., et al. 2022, MNRAS, 516, 5487  
 Lagos, P. & Papaderos, P. 2013, Advances in Astronomy, 2013, 631943  
 Lagos, P., Papaderos, P., Gomes, J. M., Smith Castelli, A. V., & Vega, L. R. 2014, A&A, 569, A110  
 Lagos, P., Scott, T. C., Nigoche-Netro, A., et al. 2018, MNRAS, 477, 392  
 Lagos, P., Telles, E., & Melnick, J. 2007, A&A, 476, 89  
 Lagos, P., Telles, E., Muñoz-Tuñón, C., et al. 2009, AJ, 137, 5068  
 Lagos, P., Telles, E., Nigoche-Netro, A., & Carrasco, E. R. 2011, AJ, 142, 162  
 Lagos, P., Telles, E., Nigoche Netro, A., & Carrasco, E. R. 2012, MNRAS, 427, 740  
 Levy, R. C., Bolatto, A. D., Sánchez, S. F., et al. 2019, ApJ, 882, 84  
 López-Cobá, C., Sánchez, S. F., Anderson, J. P., et al. 2020, AJ, 159, 167  
 Lugo-Aranda, A. Z., Sánchez, S. F., Barrera-Ballesteros, J. K., et al. 2024, MNRAS, 528, 6099  
 Luridiana, V., Morisset, C., & Shaw, R. A. 2015, A&A, 573, A42  
 Mannucci, F., Belfiore, F., Curti, M., et al. 2021, MNRAS, 508, 1582  
 Mannucci, F., Cresci, G., Maiolino, R., Marconi, A., & Gnerucci, A. 2010, MNRAS, 408, 2115  
 Marasco, A., Belfiore, F., Cresci, G., et al. 2023, A&A, 670, A92  
 Marino, R. A., Rosales-Ortega, F. F., Sánchez, S. F., et al. 2013, A&A, 559, A114  
 Martínez-Delgado, I., Tenorio-Tagle, G., Muñoz-Tuñón, C., Moiseev, A. V., & Cairós, L. M. 2007, AJ, 133, 2892  
 McClymont, W., Tacchella, S., Smith, A., et al. 2024, MNRAS, 532, 2016  
 Metha, B., Trenti, M., Chu, T., & Battisti, A. 2022, MNRAS, 514, 4465  
 Mingozi, M., Belfiore, F., Cresci, G., et al. 2020, A&A, 636, A42  
 Moiseev, A. V. & Lozinskaya, T. A. 2012, MNRAS, 423, 1831  
 Monreal-Ibero, A., Weilbacher, P. M., Micheva, G., Kollatschny, W., & Maseda, M. 2023, A&A, 674, A210  
 Papaderos, P., Guseva, N. G., Izotov, Y. I., & Fricke, K. J. 2008, A&A, 491, 113  
 Papaderos, P. & Östlin, G. 2012, A&A, 537, A126  
 Pettini, M. & Pagel, B. E. J. 2004, MNRAS, 348, L59  
 Poetrodjojo, H., D'Agostino, J. J., Groves, B., et al. 2019, MNRAS, 487, 79  
 Rand, R. J. 1998, ApJ, 501, 137  
 Sánchez, S. F. 2020, ARA&A, 58, 99  
 Sánchez, S. F., Lugo-Aranda, A. Z., Sánchez Almeida, J., et al. 2024, A&A, 682, A71  
 Sánchez, S. F., Rosales-Ortega, F. F., Iglesias-Páramo, J., et al. 2014, A&A, 563, A49  
 Sánchez, S. F., Walcher, C. J., Lopez-Cobá, C., et al. 2021, Rev. Mexicana Astron. Astrofis., 57, 3  
 Sánchez Almeida, J., Elmegreen, B. G., Muñoz-Tuñón, C., et al. 2015, ApJ, 810, L15  
 Sanders, R. L., Shapley, A. E., Topping, M. W., Reddy, N. A., & Brammer, G. B. 2023, ApJ, 955, 54  
 Schawinski, K., Thomas, D., Sarzi, M., et al. 2007, MNRAS, 382, 1415  
 Schlaflay, E. F. & Finkbeiner, D. P. 2011, ApJ, 737, 103  
 Scott, T. C., Brinks, E., Sengupta, C., & Lagos, P. 2024, A&A, 692, A51  
 Singh, R., van de Ven, G., Jahnke, K., et al. 2013, A&A, 558, A43  
 Stasińska, G., Vale Asari, N., Cid Fernandes, R., et al. 2008, MNRAS, 391, L29  
 Tomićić, N., Vulcàni, B., Poggianti, B. M., et al. 2021, ApJ, 922, 131  
 Tüllmann, R. & Dettmar, R. J. 2000, A&A, 362, 119  
 Vale Asari, N., Couto, G. S., Cid Fernandes, R., et al. 2019, MNRAS, 489, 4721  
 van Zee, L., Skillman, E. D., & Salzer, J. J. 1998, AJ, 116, 1186  
 Weilbacher, P. M., Palsa, R., Streicher, O., et al. 2020, A&A, 641, A28  
 Wiener, J., Zweibel, E. G., & Oh, S. P. 2013, ApJ, 767, 87  
 Zhang, K., Yan, R., Bundy, K., et al. 2017, MNRAS, 466, 3217

## References

Allen, M. G., Groves, B. A., Dopita, M. A., Sutherland, R. S., & Kewley, L. J. 2008, ApJS, 178, 20  
 Bacon, R., Accardo, M., Adjali, L., et al. 2010, in Society of Photo-Optical Instrumentation Engineers (SPIE) Conference Series, Vol. 7735, Ground-based and Airborne Instrumentation for Astronomy III, ed. I. S. McLean, S. K. Ramsay, & H. Takami, 773508  
 Baldwin, J. A., Phillips, M. M., & Terlevich, R. 1981, PASP, 93, 5  
 Beckwith, S. V. W., Stiavelli, M., Koekemoer, A. M., et al. 2006, AJ, 132, 1729